The Astronomical Journal, 165:74 (14pp), 2023 February https://doi.org/10.3847/1538-3881/aca64d

Kepler-102: Masses and Compositions for a Super-Earth and Sub-Neptune Orbiting an Active Star

Casey L. Brinkman[1], James Cadman[2,3], Lauren Weiss[4], Eric Gaidos[5], Ken Rice[2,3], Daniel Huber[1], Zachary R. Claytor[1], Aldo S. Bonomo[6], Lars A. Buchhave[7], Andrew Collier Cameron[8], Rosario Cosentino[9], Xavier Dumusque[10], Aldo F. Martinez Fiorenzano[9], Adriano Ghedina[9], Avet Harutyunyan[9], Andrew Howard[11], Howard Isaacson[12], David W. Latham[13], Mercedes López-Morales[13], Luca Malavolta[14,15], Giuseppina Micela[16], Emilio Molinari[17], Francesco Pepe[10], David F. Philips[13], Ennio Poretti[9,18], Alessandro Sozzetti[6], and Stéphane Udry[10]
[1] Institute for Astronomy, University of Hawai'i, 2680 Woodlawn Drive, Honolulu, HI 96822, USA; clbrinkm@hawaii.edu
[2] SUPA, Institute for Astronomy, Royal Observatory, University of Edinburgh, Blackford Hill, Edinburgh, EH9 3HJ, UK
[3] Centre for Exoplanet Science, University of Edinburgh, Edinburgh, EH9 3FD, UK
[4] Department of Physics, University of Notre Dame, Notre Dame, IN 46556, USA
[5] Department of Earth Sciences, University of Hawai'i at Mānoa, Honolulu, HI 96822 USA
[6] INAF—Osservatorio Astrofisico di Torino, via Osservatorio 20, I-10025 Pino Torinese, Italy
[7] DTU Space, National Space Institute, Technical University of Denmark, Elektrovej 328, DK- 2800 Kgs. Lyngby, Denmark
[8] SUPA School of Physics and Astronomy, University of St Andrews, North Haugh, St Andrews, KY16 9SS, UK
[9] Fundación Galileo Galilei—INAF, Rambla J.A. F. Perez, 7, E-38712 S.C. Tenerife, Spain
[10] Observatoire Astronomique de l'Université de Genéve, Chemin Pegasi 51b, CH-1290 Versoix, Switzerland
[11] Department of Astronomy, California Institute of Technology, Pasadena, CA 91125, USA
[12] 501 Campbell Hall, University of California at Berkeley, Berkeley, CA 94720, USA
[13] Center for Astrophysics | Harvard & Smithsonian, 60 Garden Street, Cambridge, MA 02138, USA
[14] Department of Physics and Astronomy, Universitá degli Studi di Padova, Vicolo dell'Osservatorio 3, I-35122 Padova, Italy
[15] INAF—Osservatorio Astronomico di Padova, Vicolo dell'Osservatorio 5, I-35122 Padova, Italy
[16] INAF—Osservatorio Astronomico di Palermo, P.za Parlamento 1, I-90134 Palermo, Italy
[17] INAF—Osservatorio Astronomico di Cagliari, via della Scienza 5 , I-09047 Selargius, Italy
[18] INAF—Osservatorio Astronomico di Brera, via E. Bianchi 46, I-23807 Merate (LC), Italy
Received 2021 December 16; revised 2022 November 4; accepted 2022 November 8; published 2023 January 27

Abstract

Radial velocity (RV) measurements of transiting multiplanet systems allow us to understand the densities and compositions of planets unlike those in the solar system. Kepler-102, which consists of five tightly packed transiting planets, is a particularly interesting system since it includes a super-Earth (Kepler-102d) and a sub-Neptune-sized planet (Kepler-102e) for which masses can be measured using RVs. Previous work found a high density for Kepler-102d, suggesting a composition similar to that of Mercury, while Kepler-102e was found to have a density typical of sub-Neptune size planets; however, Kepler-102 is an active star, which can interfere with RV mass measurements. To better measure the mass of these two planets, we obtained 111 new RVs using Keck/HIRES and Telescopio Nazionale Galileo/HARPS-N and modeled Kepler-102's activity using quasiperiodic Gaussian process regression. For Kepler-102d, we report a mass upper limit $M_d < 5.3\ M_\oplus$ (95% confidence), a best-fit mass $M_d = 2.5 \pm 1.4\ M_\oplus$, and a density $\rho_d = 5.6 \pm 3.2\ \mathrm{g\,cm^{-3}}$, which is consistent with a rocky composition similar in density to the Earth. For Kepler-102e we report a mass $M_e = 4.7 \pm 1.7\ M_\oplus$ and a density $\rho_e = 1.8 \pm 0.7\ \mathrm{g\,cm^{-3}}$. These measurements suggest that Kepler-102e has a rocky core with a thick gaseous envelope comprising 2%–4% of the planet mass and 16%–50% of its radius. Our study is yet another demonstration that accounting for stellar activity in stars with clear rotation signals can yield more accurate planet masses, enabling a more realistic interpretation of planet interiors.

Unified Astronomy Thesaurus concepts: Exoplanets (498); Super Earths (1655); Mini Neptunes (1063); Extrasolar rocky planets (511); Gaussian Processes regression (1930); Radial velocity (1332)

Supporting material: machine-readable table

1. Introduction

The results of the Kepler mission demonstrate that planets smaller than the size of Neptune form in abundance around stars like the Sun (Howard et al. 2012; Bryson et al. 2021). Half of all Sun-like stars in the Galaxy host planets between the sizes of Earth and Neptune (Petigura et al. 2013), but the Sun does not. To understand the bulk composition of these planets, for which there is no solar system analog, requires precise density estimates and planetary interior modeling.

Radial velocity (RV) measurements of transiting planets are a powerful tool to better understand the densities and compositions of other worlds. From RVs we can measure the mass of a planet, and from the transit depth we can measure its radius. Combining these gives the planet's bulk density. However, while we have many hundreds of density measurements for giant planets, and many for sub-Neptunes with radii between 1.5 and 4 $R_\oplus$, we have RV determined densities for only 42 super-Earths with radii between 1 and 1.5 $R_\oplus$ (NASA Exoplanet Archive, queried 09/14/22; Akeson et al. 2013).

In addition to the large number of RVs needed to measure the semiamplitudes produced by Earth-sized planets, starspots and active regions can affect the spectrum over time and are capable of masking the $\sim$1 m s^{-1} semiamplitudes produced by small, rocky planets. Starspots (and plage) can mimic the signature of an orbiting planet as the star rotates. If the variability of the star can be modeled along with the RV signal of the planet, the actual semiamplitude of the planet can be measured (Dumusque et al. 2011). The method of Gaussian process (GP) regression describes the correlation between data points through a covariance matrix and was introduced to the field of exoplanets in 2011 to model correlated noise from instrument systematics (Gibson et al. 2012). GP analysis was subsequently used to model correlated stellar variability due to the rotation and evolution of starspots (Haywood et al. 2014), enabling mass measurements of several small planets around active stars, including Kepler-78b (Grunblatt et al. 2016) and K2-291b (Kosiarek et al. 2019).

Another complicating factor is the degeneracy of inferring planet compositions from measured densities. We assume to first order that sub-Jovian differentiated planets are composed of an iron core, a silicate rock mantle layer, a water or ice layer, and an atmosphere likely composed of hydrogen and helium (Valencia et al. 2007). Equation-of-state modeling for silicate rock, iron, and ice allow partial constraints on possible compositions. However, it is often possible to explain the bulk density of a planet with multiple combinations of rock, metal, water/ice, and atmosphere, making the problem of finding a unique solution for composition inherently degenerate using bulk density alone (Rogers & Seager 2010). In some cases, the size and proximity of a planet to its host star can be used to justify excluding ice and atmosphere from probable compositions, since these constituents are expected to escape (Owen & Wu 2017; Lopez 2017).

From the solar system, we expect large planets to have extensive low-molecular-weight atmospheres, while smaller planets are composed primarily of rock and metal. The masses and radii of small exoplanets suggest a transition between primarily rocky and gas-enveloped planets at approximately 1.5 $R_\oplus$ (Weiss & Marcy 2014; Rogers 2015; Fulton et al. 2017), with planets smaller than 1.5 $R_\oplus$ often having compositions consistent with Earth-like iron-to-silicate ratios (Dressing et al. 2015). However, existing super-Earth mass measurements indicate a wide diversity of densities among those planets—far more diverse than we observe for rocky planets in our own solar system (Marcy et al. 2014; Morton et al. 2016; Dai et al. 2019). These RV densities suggest the interior compositions of Earth-sized planets could potentially vary from water-rich, to entirely rocky, to predominantly iron (Bonomo et al. 2019).

Above $R = 1.5\ R_\oplus$, planets tend to retain substantial H/He envelopes that increase the radius while decreasing the density. Neptune is often called an "ice giant" planet, and initially many sub-Neptune size exoplanets were also modeled as icy planets. However, many studies now argue that they are alternatively composed of a solid core with a gaseous envelope (Rogers 2015; Owen & Wu 2017), while others argue they are water worlds (Zeng et al. 2019). Some recent studies have even suggested deep magma oceans for many sub-Neptunes discovered by Kepler, which we expect to greatly impact the composition of the atmosphere (Kite et al. 2020).

Table 1
Kepler-102 Stellar Properties

Kepler-102 Stellar Properties		
Property	Value	Source
Other names	KOI 82	B
KIC ID	10187017	B
R.A. (J2000)	18 45 55.85	B
decl. (J2000)	+47 12 28.84	B
V (mag)	12.07	B
$T_{\rm eff}$ (K)	4909 ± 98	F
Metallicity [Fe/H]	0.11 ± 0.04	F
Mass ($M_\odot$)	0.803 ± 0.021	F
Radius ($R_\odot$)	0.724 ± 0.018	F
Isochrone age (Gyr)	$1.07^{+3.6}_{-0.5}$	F
Rotation-based age (Gyr)	4.5 ± 1.1	*
Trigonometric parallax (mas)	9.301 ± 0.019	F

Note. Stellar properties for Kepler-102 compiled from the following sources: B = Brown et al. (2011), F = Fulton & Petigura (2018), * = this work.

An interesting system for exploring planet compositions is Kepler-102, which consists of five tightly packed transiting planets (within 0.16 au of their host star), including a super-Earth and a sub-Neptune-sized planet. Previously, masses have been measured for the super-Earth Kepler-102d ($M_d = 3.8 \pm 1.8\ M_\oplus$) and sub-Neptune Kepler-102e ($M_e = 8.93 \pm 2.0\ M_\oplus$; Marcy et al. 2014). The density of Kepler-102d was found to be $\rho_e = 13.3 \pm 6.46$ g cm^{-3}, suggesting the planet was consistent with a composition of pure compressed iron. Kepler-102e was found to have a density consistent with other sub-Neptunes. Marcy et al. (2014) did not report masses for the other three planets, which are all smaller than the Earth.

The radius of Kepler-102 was recently revised by Fulton et al. (2018) using the Gaia parallax, yielding more accurate and precise measurements for the radii of all transiting planets in the system. The density of Kepler-102d dropped from $\rho_d = 13.3$ to $\rho_d = 9.5$ g cm^{-3}, allowing the planet to have a mixed composition of iron and rock. While this revised density is more realistic, it is still high for a planet of its size, implying a Mercury-like composition.

Kepler-102, however, is an active star, as indicated by a Mt. Wilson S-value of 0.41 (Schröder et al. 2013) and logR'HK of -4.6, and such activity could potentially interfere with the previous mass measurements for Kepler-102d and Kepler-102e. In this work, we present new mass and density measurements for these planets, using new RVs from Keck/HIRES and Telescopio Nazionale Galileo (TNG)/HARPS-N and applying GP regression to model the stellar activity in both the photometry and the RVs. We then explore new composition estimates using equation-of-state modeling.

2. Stellar Activity and Rotation

2.1. Kepler Photometry

The Kepler spacecraft, launched in 2009, observed one >100 square degree patch of the sky continuously until 2013, looking for the signatures of transiting exoplanets (Borucki et al. 2010). Photometry of Kepler-102 was gathered at a 30 minutes cadence for 17 quarters of observations. The properties of Kepler-102 are given in Table 1.

Table 2
Kepler-102 Planet Properties

Kepler-102 Planet Properties				
Planet Name	Period (days)	T_c (days)	Radius ($R_\oplus$)	Mass ($M_\oplus$)
Kepler-102b	5.28697 ± 0.00001 [G]	2454968.870 ± 0.001 [G]	0.471 ± 0.024 [F]	⋯
Kepler-102 c	7.07139 ± 0.00002 [G]	7.07139 ± 0.00002 [G]	0.554 ± 0.026 [F]	⋯
Kepler-102d	10.311767 ± 0.000004 [G]	2454967.0913 ± 0.0001 [G]	1.340 ± 0.089 [F]	2.5 ± 1.4 [*]
Kepler-102e	16.145699 ± 0.000002 [G]	2454967.7537 ± 0.0001 [G]	2.414 ± 0.142 [F]	4.7 ± 1.7 [*]
Kepler-102f	27.45359 ± 0.00006 [G]	2454978.028 ± 0.001 [G]	0.753 ± 0.033 [F]	⋯

Note. Parameters for the Kepler-102 system compiled from the following sources: G = Gajdos et al. (2019), F = Fulton & Petigura (2018), * = this work.

To assess whether the photometry of Kepler-102 showed the quasiperiodic rotational modulation characteristic of active stars, we downloaded the Kepler Pre-search Data Conditioning SAP (PDCSAP) flux photometry using the package `Lightkurve` (Lightkurve Collaboration et al. 2018). In our analysis we used the full 17 quarters of photometry on Kepler-102, and we masked out the individual transits of Kepler-102d and Kepler-102e using their orbital periods and conjunction times (Table 2). The transit depths for the other three planets were negligible. We furthermore rebinned the photometry to have one data point every 10 hr to make our computations more manageable. While this removes information about stellar variability on timescales shorter than this, 10 hr is much less than the expected stellar rotation period and the starspot decay timescale. Figure 1 shows the full Kepler light curve over all 17 quarters. We observe a distinct rotation signal, consistent with the presence of starspots.

We computed a rotation-based age for Kepler-102 using the stellar model grid-fitting tools in `kiauhoku` (Claytor et al. 2020). Using the magnetic rotational braking law of van Saders & Pinsonneault (2013), we derived an age of 4.5 ± 1.1 Gyr. We note that using the stalled braking law of van Saders et al. (2016) did not significantly affect the age estimate. This is consistent with the isochrone age from Fulton & Petigura (2018) to within 1σ.

2.2. Gaussian Process Model

We use GP regression to characterize the stellar noise caused by the rotation of starspots and plage (Rasmussen & Williams 2006). A commonly used model for this type of stellar noise is quasiperiodic: the rotation of the star produces a periodic signal, but evolution of starspots adds gradual phase offsets to the periodic signal. To capture this behavior we use the quasiperiodic kernel from the `RadVel` package (Fulton et al. 2018), the product of a periodic function and a squared exponential function, given as

$$C_{ij} = \eta_1^2 \exp\left[-\frac{|t_i - t_j|^2}{\eta_2^2} - \frac{\sin^2(|t_i - t_j|/\eta_3)}{2\eta_4^2}\right], \quad (1)$$

where η_1 is the amplitude of the covariance, η_2 is the timescale of the exponential decay (here a proxy for the spots evolutionary timescale), η_3 is the variability period (here the rotational period of the star), and η_4 is a coherence scale for the periodic variability. The terms i and j are the indices of the covariance matrix.

GPs are nonparametric, meaning that they do not produce a predictive model of the data using fitting parameters. Instead, they use tunable hyperparameters, which inform how the GP fits the covariance kernel to the data. In this analysis η_1, η_2, η_3, and η_4 are hyperparameters for the quasiperiodic kernel.

The flexibility of GPs is a double-edged sword: GPs can be used to describe complex data sets that more traditional modeling cannot, but they also have ability to overfit the data, resulting in the unintentional removal of planetary signals. One method of mitigating the overfitting of data is to ensure that the GP has physically motivated priors for each hyperparameter.

2.3. Determining Gaussian Process Priors

The rotation and evolution of starspots will produce similar signals in photometry and in the RVs. The rotational period of the star, the exponential decay timescale, and coherence scales should be consistent between photometry and RVs, while the amplitudes of each signal are in different units and should not be consistent. Therefore, we can use the posterior results of the photometric fit as physically motivated starting values for η_2, η_3, and η_4. This should help the GP to distinguish between the stellar and planetary signals present in the RVs. The light curve is an ideal data set for this training because it is sampled at a much higher cadence than the sparse RV curve, which allows us to more accurately determine the hyperparameters.

Before fitting the light curve, we derived a starting value for the rotation period of the star by looking at the period of maximum power using a wavelet transform (Figure 2). We used the Morlet wavelet transform from Virtanen et al. (2020) in SciPy, and applied the power spectral density correction from Liu et al. (2007). We observe a strong peak in the time-integrated power spectrum at ∼27 days, which we interpret as the rotation period of the star. Through the entire light curve, however, we can see a very pronounced evolution of the stellar activity through the change in periods that show significant power. In the first four quarters, the period of maximum power appears distinctly as ∼13 days without power at 27 days. This is indicative of spots on either side of the star, as they make the rotation period appear as half its value for the first four quarters, before one of the spots disappears (Haywood et al. 2014; Berger et al. 2018).

First, we fit each of the 17 quarters of photometry separately because as the light curve evolves, so can the hyperparameters. Equation (1) is not sufficient to model a star that has spots with different decay timescales and rotation periods (e.g., latitudinal differential rotation), therefore fitting each quarter separately informs us of the variance in these timescales. The best-fit hyperparameters for each quarter are given in Table 3. We found that part of the light curve has a best-fit exponential decay length (η_2) of ∼30–34 days, while the other parts a best-fit value of ∼22–28 days.

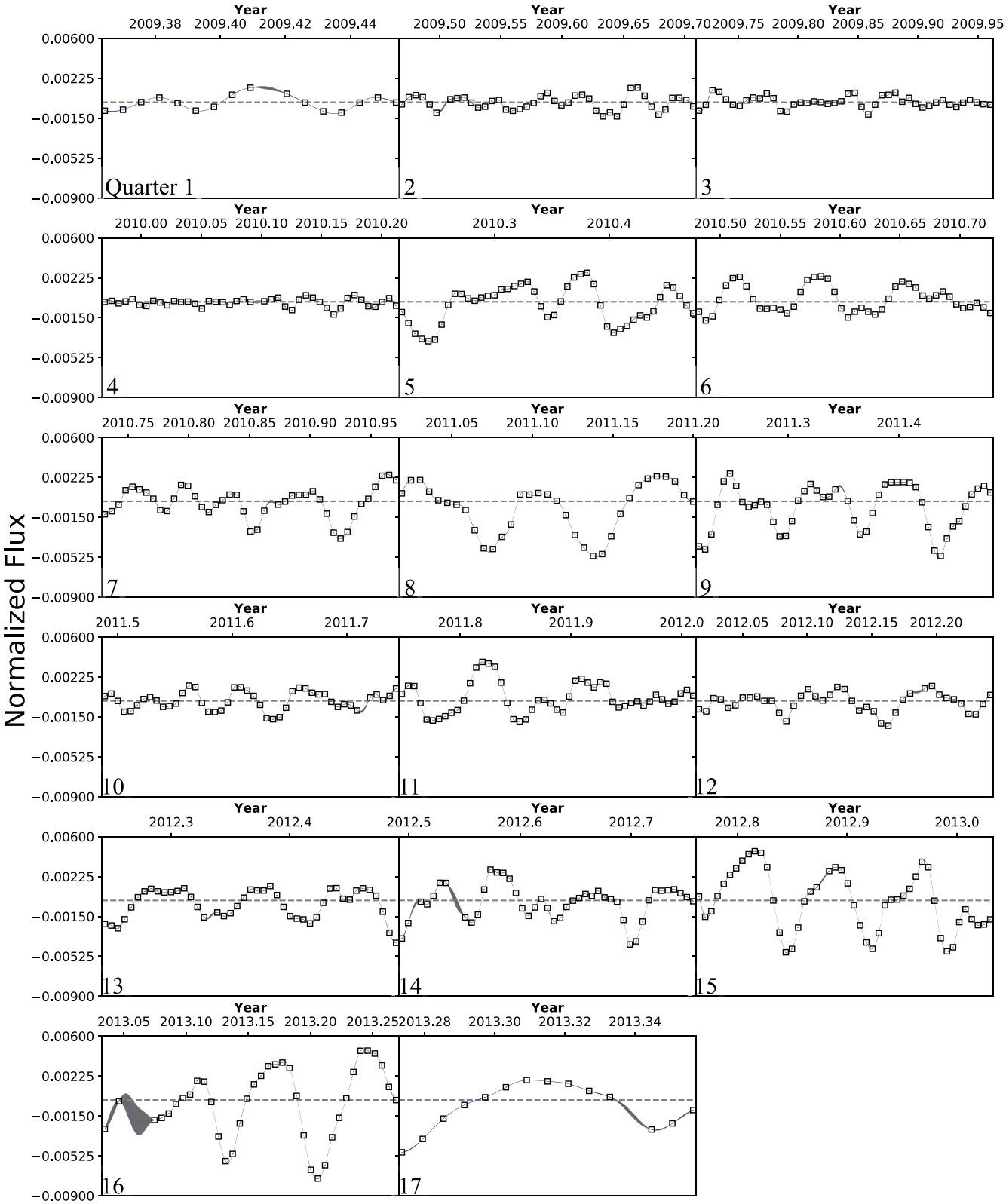

Figure 1. PDCSAP flux of Kepler-102 over 17 quarters of observation, binned every 10 hr (open boxes). Each panel corresponds to one quarter of photometry. The blue curve shows the Gaussian process (GP) regression of the photometry with the best-fit kernel hyperparameters from Table 5. The gray shaded regions show the uncertainty in the GP model.

We then fit the full Kepler photometry to determine the best overall hyperparameters, listed in Table 5. The best-fit η_1, η_3, and η_4 are similar to the median of the individual 17 quarters fits. The best-fit η_2 (30 days) is not the same as the median of the 17 individual quarters (26 days), but falls within 1σ of this value. We will use the hyperparameters from the full light-curve fit for the starting values in the RV fit, with a cautious treatment of η_2, as discussed later.

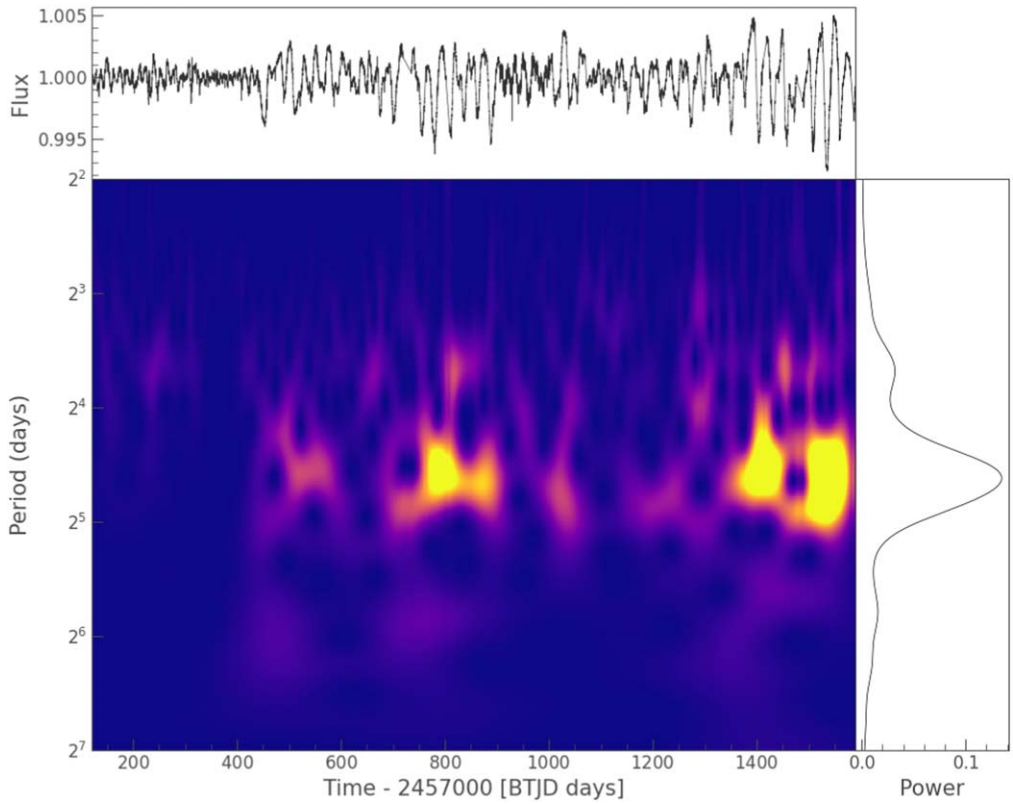

Figure 2. Wavelet analysis for the 4 yr light curve of Kepler-102. The top panel shows the photometry over 17 quarters of Kepler data, where time is measured in Barycentric TESS Julian Date. The central panel shows the time-variable frequency decomposition. The right panel shows the time-integrated wavelet power spectrum of the light curve. The clear period of maximum power is at 27 days, suggesting that this is the rotation period of the star, which we use to inform our GP kernel. There is also significant power from 10 to 32 days, showing that spots form, evolve, and disappear over time. The peak at 13 days is likely a half-period alias from spots appearing on opposite sides of the star (Haywood et al. 2014; Basri & Nguyen 2018).

Table 3
GP Hyperparameters by Kepler Quarter

GP Hyperparameters by Kepler Quarter				
Q	η_1 (Flux $\times$ 10^{-3})	η_2 (Days)	η_3 (Days)	η_4
1	1.0 ± 0.1	29 ± 3	26 ± 1	0.032 ± 0.06
2	0.6 ± 0.08	28 ± 5	27 ± 1	0.34 ± 0.08
3	0.5 ± 0.08	25 ± 4	26 ± 0.4	0.21 ± 0.01
4	0.38 ± 0.08	23 ± 2	26 ± 0.5	0.13 ± 0.02
5	1.5 ± 0.2	27 ± 2	26 ± 0.9	0.28 ± 0.02
6	0.99 ± 0.2	34 ± 4	26 ± 0.2	0.22 ± 0.01
7	1.2 ± 0.2	32 ± 5	27 ± 1	0.22 ± 0.02
8	1.9 ± 0.4	31 ± 6	26 ± 0.3	0.29 ± 0.02
9	1.6 ± 0.3	35 ± 5	26 ± 0.4	0.31 ± 0.03
10	0.77 ± 0.6	22 ± 6	26 ± 1	0.26 ± 0.04
11	1.3 ± 0.1	23 ± 3	26 ± 0.8	0.28 ± 0.01
12	0.79 ± 0.1	23 ± 3	26 ± 0.9	0.16 ± 0.01
13	1.2 ± 0.2	28 ± 4	26 ± 0.3	0.23 ± 0.02
14	1.3 ± 0.2	24 ± 3	26 ± 0.9	0.16 ± 0.01
15	2.0 ± 0.2	37 ± 4	26 ± 0.2	0.25 ± 0.01
16	2.3 ± 0.4	34 ± 5	26 ± 1	0.18 ± 0.01
17	2.0 ± 0.6	54 ± 20	26 ± 0.5	0.26 ± 0.2

Note. Best-fit hyperparameters for the quasiperiodic Kernel shown for each quarter of Kepler photometry fit seperately. η_1 corresponds to the amplitude of covariance in normalized flux, η_2 to the exponential characteristic length, η_3 to the period of covariance (here, the rotation period of the star), and η_4 to the periodic coherence scale.

Figure 1 shows the photometry with the GP regression using the best-fit hyperparameters listed in Table 5.

We also used a quasiperiodic kernel to fit the Kepler photometry in `PyORBIT` (Malavolta et al. 2016, 2018), a package for modeling planetary and stellar activity signals. The GP quasiperiodic kernel was applied through the `george` package (Ambikasaran et al. 2015). Hyperparameter optimization was performed using the differential evolution code `pyDE`. The optimized hyperparameters were then given as priors to the affine-invarient ensemble sampler `emcee` (Foreman-Mackey et al. 2013), from which we obtained our best-fit activity parameters. The best-fit values for the hyperparameters obtained from PyORBIT were found to agree well with those found using `RadVel`.

3. Planet Masses

3.1. Radial Velocity Data

3.1.1. HIRES

We make use of 72 RVs from the HIRES echelle spectrometer on the 10 m Keck I telescope (Vogt et al. 1994). Marcy et al. (2014) obtained data between 2010 and 2013, totaling 35 RVs. The California Planet Search (CPS) team collected 37 additional RVs spanning 2013–2019 (L. M. Weiss et al. 2023, in preparation).

The spectrometer uses an iodine cell mounted in front of the slit in order to provide a benchmark spectrum against which the Doppler shift of Kepler-102 can be measured. The resulting

Table 4
Kepler-102 RVs

Time (BJD)	RV ($m\,s^{-1}$)	RV unc ($m\,s^{-1}$)	Activity Indicator		Telescope
			S-index	FWHM	
2455312.08	−3.89	1.53	0.4420		HIRES
2455373.83	−3.36	1.57	0.4130		HIRES
2456245.38	−2.86	2.84		7629	HARPS-N
2456397.61	4.52	2.30		7767	HARPS-N

Note. A few lines of our RV table are shown here. The activity indicator reported for HIRES values is the *S*-index while the activity indicator reported for HARPS-N values is the FWHM.

(This table is available in its entirety in machine-readable form.)

shapes of the iodine lines account for changes in spectrometer optics by recording the point-spread function (PSF) of the spectrometer (Marcy & Butler 1992). We obtained a template spectrum by observing the star without the iodine cell. To model the PSF of the HIRES spectrograph we also observed rapidly rotating B stars with the iodine cell in the light path immediately before and after the template. Each RV spectrum was then reproduced with the deconvolved template spectrum and a laboratory iodine atlas spectrum convolved with the HIRES PSF of the observation. Sky subtraction was performed through the use of a 14.″0 long slit in order to observe enough sky compared to the Keck PSF (FWHM = 1.″0) to get a robust background estimate. We used the standard CPS data-reduction pipeline as described in Howard et al. (2010).

3.1.2. HARPS-North

We obtained a total of 78 RVs for Kepler-102 using the HARPS-N spectrograph installed on the 3.6 m TNG at the Observatorio Roque de Los Muchachos in La Palma, Spain. These were collected as part of the HARPS-N Collaboration's Guaranteed Time Observations program, and span a period from 2012 June to 2020 July. The RVs are listed in Table 4.

A CCD change after the observation at BJD 2456162.45 meant that we separated the 78 RVs into two distinct data sets in order to account for this change. We collected a total of 23 RVs prior to the CCD change and 55 afterwards. Each of these observations had an exposure time of 1800 s. The spectra prior to the CCD change were reduced using the HARPS-N Data Reduction Software (DRS) 3.7. The spectra after the CCD change were reduced using the new DRS 2.2.8 (Dumusque et al. 2021).

We discovered anomalously large uncertainties in three of the RVs at BJD = 2456102.48, 2456606.34, and 2456606.37, most likely due to poor seeing according to the observing logs, and we therefore excluded them from our analysis. With the exception of these, our remaining 22 observations prior to the CCD change had signal-to-noise ratio (S/N) values between 24.8 and 54.4 per extracted pixel, with an average value of 41.2 at 550 nm and a mean RV precision of 2.14 $m\,s^{-1}$. The remaining 53 RVs after the CCD change had S/N values between 19.72 and 67.12 per extracted pixel, with an average value of 49.63 at 550 nm and a mean RV precision of 2.27 $m\,s^{-1}$.

3.2. Simple Keplerian Orbital Fit

We used the open source Python package `RadVel` (Fulton et al. 2018) to model the RVs. We first attempted to measure the masses of Kepler-102d and Kepler-102e by fitting a Keplerian orbit only, in which the RV curve is described by the orbital period, conjunction time, eccentricity, argument of periastron, and RV semiamplitude of each planet. We include two additional terms to fit the RVs: a zero-point offset (γ) and a RV jitter term (σ_j) for each data set (and two for HARPS-N before and after the CCD change). Jitter accounts for additional Gaussian and non-Gaussian noise that can be astrophysical in origin or can come from systematics of the spectrograph. This additional uncertainty gets added in quadrature with the intrinsic uncertainties on the RVs to minimize the likelihood function. The likelihood function used in `RadVel` is

$$\ln(\mathcal{L}) = -\sum_i \frac{(v_i - v_m(t_i))^2}{2(\sigma_i^2 + \sigma_{\rm jit}^2)} - \ln\sqrt{2\pi(\sigma_i^2 + \sigma_{\rm jit}^2)}, \quad (2)$$

where $\mathcal{L}$ is the likelihood, v_i and σ_i are the ith RV measurement and its associated uncertainty, $v_m(t_i)$ is the Keplerian model RV at time t_i, and $\sigma_{\rm jit}$ is the jitter estimate.

We fit the RV curve in terms of the two larger planets in the system on Keplerian orbits. We used the published inclinations of the planets, and assumed eccentricities $e = 0$, based on findings that the eccentricities in compact, high-multiplicity coplanar systems tend to be significantly lower than what is required for dynamical stability (e.g., Yee et al. 2021). The orbital periods and conjunction times are precisely known from Kepler and were therefore fixed in our analysis (Marcy et al. 2014; Gajdos et al. 2019). After optimizing for the maximum-likelihood fit, we ran `RadVel`'s built-in Markov Chain Monte Carlo (MCMC) algorithm (Foreman-Mackey et al. 2013) to explore the surrounding parameter space and estimate the uncertainty in the model parameters, and to explore the covariance between parameters.

We fit the HIRES and HARPS-N data first separately, and then together for Kepler-102d and Kepler-102e. The semi-amplitudes for each fit, the resulting masses, and the bulk densities of each planet are listed in Table 6.

While the uncertainties for the mass of Kepler-102d are large, comparing the best-fit values obtained with each data set is useful to understand the potential effects of stellar variability on the RVs. The HIRES data produces a mass upper limit, defined as the 95th percentile of the posterior distributions, $M_d < 8.3\ M_\oplus$, and best-fit mass $M_d = 4.5 \pm 1.9\ M_\oplus$. This translates to a best-fit density $\rho_d = 10 \pm 5\ {\rm g\,cm^{-3}}$. The HARPS-N data, on the other hand, produces an upper mass limit $M_d < 3.9\ M_\oplus$, a best-fit mass $M_d = 0.7 \pm 1.6\ M_\oplus$, and a density $\rho_d = 2 \pm 4\ {\rm g\,cm^{-3}}$. While these best-fit masses are only $\sim 1.5\sigma$ apart due to large uncertainties, one suggests a composition similar to Mercury, while the other suggests an extensive volatile envelope. Combining the data sets gives a mass upper limit $M_d < 5\ M_\oplus$, a best-fit mass $M_d = 2.4 \pm 1.3\ M_\oplus$, and a density $\rho_d = 5.4 \pm 3.0\ {\rm g\,cm^{-3}}$. This is a density typical of rocky planets; however, it is the result of combining the large density measured from HIRES with the low density measured from HARPS-N. We discuss attempts to reconcile the different RV results in Sections 3.3 and 3.4.

For Kepler-102e, the best-fit values of the semiamplitude based on each individual data set, and combined data sets, are listed in Table 6. These are used to calculate a mass $M_e = 5 \pm 2$

Table 5
GP Kernel Hyperparameters

Gaussian Process Kernel Parameters		
Parameter	Light Curve Fit	Radial Velocities Fit
η_1 (flux, m s^{-1})	0.0012 ± 0.0006	2.4 ± 0.4
η_2 (days)	30 ± 6	31 ± 2
η_3 (days)	26 ± 1	27 ± 1
η_4	0.2 ± 0.1	0.3 ± 0.1

Note. The best-fit hyperparameters for the quasiperiodic kernel are shown for both the photometric and RV GP regression.

$M_\oplus$ and a density $\rho_e = 2 \pm 1$ g cm^{-3} using HIRES, and a mass $M_e = 3 \pm 2\ M_\oplus$ and a density $\rho_e = 1 \pm 1$ g cm^{-3} using HARPS-N. These values differ from each other by 1σ.

To test the robustness of our two-planet model, we varied the number of planets included. We use the Bayesian Information Criterion (hereafter, BIC) to compare models of this system with two versus five planets. The BIC rewards models that fit the data well (based on optimizing a likelihood function), but also penalizes models based on the number of free parameters. Thus, the BIC can be used to select the simplest model that adequately describes the data. The BIC is defined as

$$\mathrm{BIC} = \ln(n)k - 2\ln(\mathcal{L}_{\max}), \tag{3}$$

where n is the number of data points, k is the number of free parameters, and $\mathcal{L}_{\max}$ is the maximum value of the likelihood function for the model (Kass & Raftery 1995).

We find that the model with two planets produces a BIC of 822, while the model with five planets produces a BIC of 831. A ΔBIC of 9 indicates the two-planet fit is preferred. This does not suggest that there are only two planets in the system, since we know of five transiting planets. It is unsurprising that these three planets are not contributing to the fit, since we would expect their semiamplitudes to range from 0.03 to 0.09 m s^{-1}, assuming masses from the Weiss & Marcy (2014) mass–radius relation.

3.3. Gaussian Process Radial Velocity Fit

Despite the fact that the combined data set produces a reasonable mass for Kepler-102d, it prompts the question: Why are the best-fit semiamplitudes to the HIRES and HARPS-N data sets so discrepant? One potential reason is stellar activity, which can create time-dependent offsets in the RVs for each data set. This is not the first time discrepant mass values have been found for exoplanets with HIRES and HARPS-N, another example being Kepler-10 (Dumusque et al. 2014; Weiss et al. 2016).

To improve our understanding of the system, we applied our knowledge of the stellar activity to construct a physically motivated GP model for the RV variability. We used the posterior values for η_2, η_3, and η_4 from our photometric fit (see Section 2.3, values listed in Table 5) as the starting values for a new quasiperiodic kernel, fitting the GP now to the RVs. Because the best-fit values for exponential length η_2 varied from 22 to 37 days in the photometric fit, we fit the RVs with four different starting values for η_2: 22, 27, 31, and 37, which were allowed to vary. The values for the semiamplitude of each planet remained constant with differing values for η_2. We used 31 days for the fit presented here, but note that any of these values for η_2 would produce the same result.

In addition to using the photometric fit as starting values, we used Gaussian priors on each value centered on the photometric best fit with uncertainties from the photometric fit. To ensure that using the priors for the hyperparameters on the stellar activity, obtained from the photometry in Section 2.3, are not leading to overfitting of the RVs, we performed some additional tests with loosened constraints on the activity. Specifically, we removed priors on η_2 and η_4, hence only constraining the rotation period, η_3. When doing this, the masses of Kepler-102d and Kepler-102e remain consistent with those quoted in Table 6.

In addition to the GP stellar noise model, we include a Keplerian RV model for the planets (as described above) and fit for both planetary and stellar signals simultaneously. We included only the two largest planets because our previous BIC analysis demonstrated that the goodness of fit did not benefit from incorporating the three smaller planets. The results of this fit are shown in Figure 3, and the best-fit values for each planet are given in Table 6.

The best-fit GP hyperparameters from the posterior of the RV fit are shown in Table 5 together with those from the photometric fit. The parameter with the largest difference between the photometry and RV fits is the variability amplitude. This is expected because the amplitude of the photometry is in units of normalized flux, while the amplitude of the RVs is meters per second, and therefore should not be comparable.

We also used `PyOrbit` (Malavolta et al. 2016, 2018), utilizing the affine-invariant ensemble sampler `emcee`, and a differential evolution-MCMC technique (Eastman et al. 2013; Bonomo et al. 2015) to independently fit the RVs. We recovered values within 1σ of the values found with `RadVel` for the semiamplitudes of each planet and for the hyperparameters. The values listed in Tables 5 and 6 are those found using `RadVel`.

We calculate the BIC of the fit before and after using GP regression to model stellar variability and find that it drops from 822 to 819. A $\Delta\mathrm{BIC} = 3$ corresponds with positive evidence that the lower BIC model is a better fit relative to the number of free parameters (Lorah & Womack 2019), meaning here that the model that includes GP regression for stellar noise is preferred by the BIC even though it includes four additional free parameters. The BIC is not our only metric of determining the validity of the GP: we know from the photometry and the Mt. Wilson S-value that Kepler-102 shows clear signs of starspots and rotation, and therefore the use of the GP is physically motivated. We also note that Lomb–Scargle periodograms of the activity indicators for both data sets (S-index for HIRES, FWHM for HARPS-N) show periodicity at one quarter the rotation period of the star (6.5 days), and the S-index from HIRES shows periodicity at the full rotation period of the star (25 days), as shown in Figure 4. This suggests that RV variability on the timescale of the rotation period of the star is present in the RVs, and supports the usage of a quasiperiodic GP.

A common concern is that the GP can remove the planetary signal. To ascertain whether this was the case in Kepler-102, we examined the covariance between the planet and the GP hyperparameters (Figure 5). We observe that the semiamplitudes for the planets are uncorrelated with the GP hyperparameters, indicating that the GP is not artificially reducing nor inflating the semiamplitude of either planet. This, combined

Table 6
Model Comparison

Model Comparison							
Parameter	Previous Value	HIRES without GP	HIRES with GP	HARPS-N without GP	HARPS-N with GP	Full Data Set without GP	Full Data Set with GP
Kepler-102d K ($m\,s^{-1}$)	1.4 ± 0.6	1.5 ± 0.7	0.9 ± 0.7	0.25 ± 0.5	0.8 ± 0.5	0.8 ± 0.4	0.9 ± 0.5
Kepler-102d mass ($M_\oplus$)	3.8 ± 1.8	4.5 ± 1.9	2.7 ± 2.1	0.7 ± 1.6	2.3 ± 1.4	2.4 ± 1.3	2.5 ± 1.4
Kepler-102d density (g/cm^3)	9.5 ± 6.5	10.1 ± 4.5	6.2 ± 4.7	1.7 ± 3.9	5.6 ± 3.4	5.4 ± 3.0	5.6 ± 3.2
Kepler-102e K ($m\,s^{-1}$)	2.8 ± 0.6	1.4 ± 0.6	1.6 ± 0.7	0.8 ± 0.6	1.2 ± 0.7	1.2 ± 0.4	1.4 ± 0.5
Kepler-102e mass ($M_\oplus$)	8.9 ± 2.0	4.8 ± 2.1	5.3 ± 2.2	2.8 ± 1.9	4.1 ± 2.2	4.0 ± 1.4	4.7 ± 1.7
Kepler-102e density (g/cm^3)	3.5 ± 1.1	1.9 ± 0.8	2.7 ± 0.8	1.1 ± 0.8	1.6 ± 0.8	1.6 ± 0.6	1.8 ± 0.7
RV jitter ($m\,s^{-1}$)		2.4 ± 0.5	1.8 ± 0.4	2.9 ± 0.8	1.9 ± 1.0	3.6 ± 0.5[a] 2.1 ± 1.0[b]	2.5 ± 0.5[a] 2.0 ± 1.0[b]
BIC	N/A	421	418	399	405	822	819

Notes. The semiamplitudes, masses, and densities of Kepler-102d and Kepler-102e across different models and data sets are given above. Previously published masses are taken from Marcy et al. (2014), and densities are calculated using the radii from Table 2. All models include only the two largest of the five planets in the system. We adopt the values obtained from the Full Data set with the GP as the semiamplitudes, masses, and densities for the planets.
[a] Jitter key: a = jitter values for the HIRES data set.
[b] b = jitter values for the HARPS-N data set.

with our exploration of the exponential decay timescale η_2 (discussed above), gives us confidence that the GP is only fitting the stellar noise, and that our measured semiamplitude reflects the portion of the RV variations due to the orbit of the planets.

3.4. Discussion

After accounting for stellar noise, the semiamplitude for Kepler-102d is only marginally detected, with $\sim 2\sigma$ significance, with an upper limit on the mass of $M_d < 5.3\ M_\oplus$ (calculated as the 95th percentile of the posterior distributions). The best-fit semiamplitude of Kepler-102d is $K_d = 0.9 \pm 0.5\ m\,s^{-1}$. This results in a mass $M_d = 2.5 \pm 1.4\ M_\oplus$ compared to the previously published value of $3.8 \pm 1.8\ M_\oplus$. Using the planet radius from Table 2, we get a density $\rho_d = 5.6 \pm 3.2\ g\,cm^{-3}$, roughly half the previously measured density of $9.5\ g\,cm^{-3}$. The density measurements from the separate HIRES and HARPS-N data sets produce values within 1σ of each other and the combined data set using a GP stellar noise model, while they both differ by $>1\sigma$ from each other and from the combined data set without using a GP. Accounting for stellar variability appears to partly reconcile the difference in mass measurements from HIRES and HARPS-N, suggesting that stellar activity could be the source of the discrepant measurements.

The best-fit semiamplitude for Kepler-102e in the two-planet fit with GP regression is $K_e = 1.4 \pm 0.5\ m\,s^{-1}$. The resulting mass for this planet is $M_e = 4.7 \pm 1.7\ M_\oplus$, lighter than the previously published mass of $8.9\ M_\oplus$ (Marcy et al. 2014). Using the radius of this planet (Table 2), we find a density $\rho_e = 1.8 \pm 0.7\ g\,cm^{-3}$, compared to the $4.7\ g\,cm^{-3}$ published previously. The density measurements for this planet made using the separate HARPS-N and HIRES data sets, both with and without the GP model, fall within 1σ of this measurement.

Figure 6 places our new mass and density measurements for the Kepler-102 planets in context with the RV-measured densities of other planets. The sample contains all planets with radii $R < 4\ R_\oplus$ and published RV mass measurements (NASA Exoplanet Archive, queried 10/01/21; Akeson et al. 2013). We excluded planets with upper-limit mass values only, or mass measurements from transit timing variations. The mass–radius and density–radius trends for rocky and gaseous planets from Weiss & Marcy (2014) are also included, along with mass–radius and density–radius curves for planets of different compositions from Zeng et al. (2019).

The density of Kepler-102d using the combined data set and GP stellar noise modeling falls below the trend for average planet density at its given radius, while the uncertainty on this measurement places it within 1σ of this relation. The density of Kepler-102e using the full data set and GP modeling falls below the average density relation for sub-Neptunes, but is also consistent with it to within 1σ.

The wide variety of densities found using different data sets and models illustrates the difficulty of measuring precise densities for small planets. However, the individual data sets used without GPs fall the furthest away from the expected density range for rocky planets, while those same data sets used with GPs fall much closer to that range and fall closer to each other and the combined data set. This suggests that the GP analysis helps with constraining more accurate densities for rocky planets, and should be implemented with care for systems with clear signals of rotation and activity in the host star.

4. Planet Compositions

4.1. Planet Interior Modeling

We combined our mass and radius measurements of Kepler-102d and 102e with models of the interior structures of differentiated rocky planets to constrain their compositions. We assumed the planets are differentiated, a consequence of energy released and melting occurring during accretion (Chao et al. 2021), but the mass–radius relation of rocky planets is not very sensitive to their degree of differentiation (Elkins-Tanton & Seager 2008). We also ignored the contribution of any atmosphere to the radius, but this could be significant in the case of thick hydrogen-helium envelopes. By ignoring such atmospheres we estimated maximum model masses; a model mass that significantly exceeds the measured value for the lightest plausible composition indicates that such an atmosphere is present.

Our modeling used `BurnMan 0.9` (Cottaar et al. 2016), which takes user-provided equations of state (EOS) and the

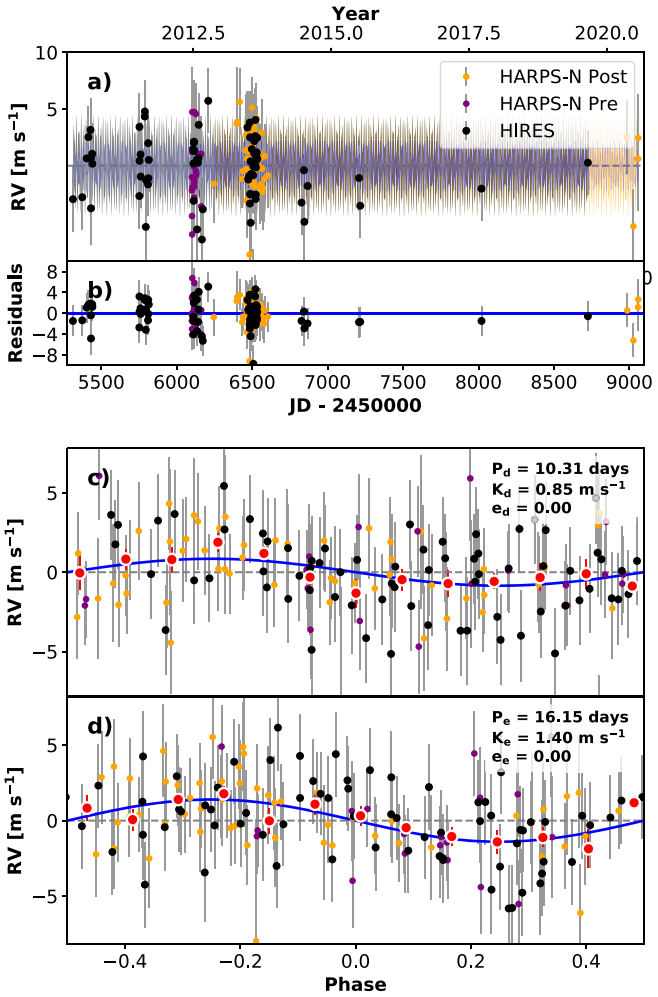

Figure 3. Combined Keplerian orbit model for the planets and Gaussian process (GP) stellar noise fit. The best-fit kernel priors were found using the Kepler photometry in Figure 1 before application to the radial velocities (RVs). (a) RV vs. time as observed by HIRES and HARPS-North (pre and post CCD upgrade) are plotted with 1σ uncertainties. The blue line represents the total model of the planets and the GP regressions, with the gray region showing 1σ uncertainties. (b) Residuals of the model subtracted from the RVs. (c) The phase-folded RVs for Kepler-102d with the best-fit semiamplitude model overplotted. The red points are phase-folded weighted-mean RVs and their uncertainties. (d) Same as (c) but for Kepler-102e.

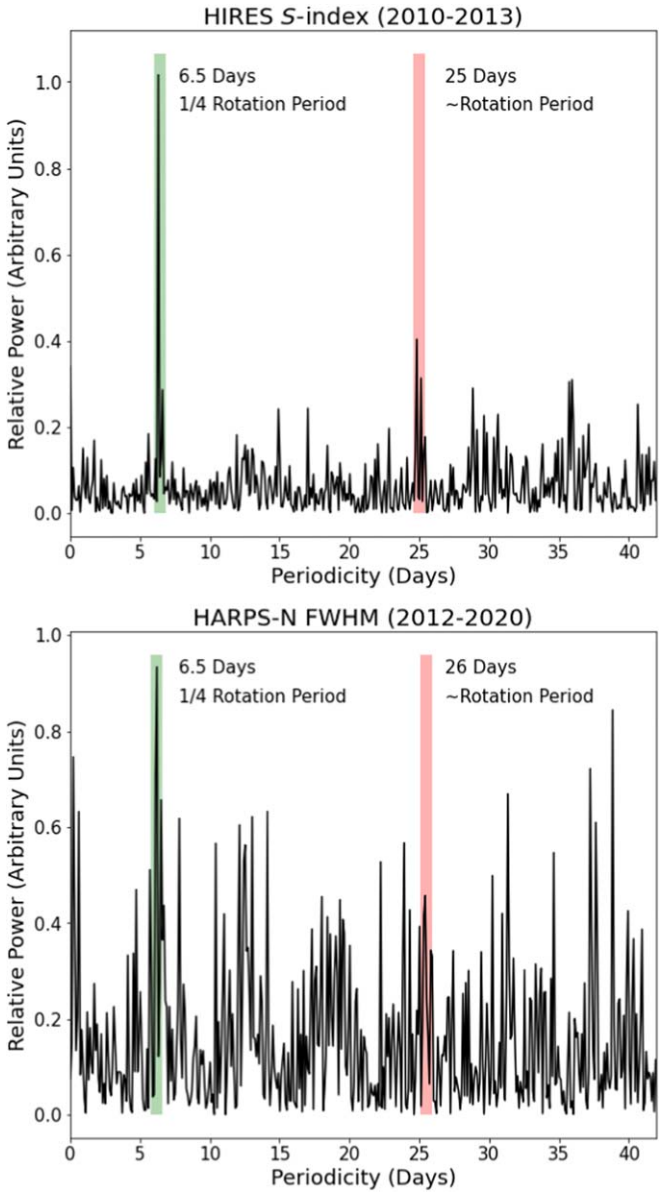

Figure 4. Lomb–Scargle periodograms (LSPs) of the activity indicators for each radial velocity (RV) data set (*S*-index for HIRES, FWHM for HARPS-N) show a notable peak at 6.5 days, which is one quarter the rotation period (or third harmonic of the rotation period) of the star. In the HIRES *S*-index LSP we identify a very tentative signal at 25 days (within one standard deviation of the rotation period of the star), while in the HARPS-N FWHM LSP there is not an identifiable signal at the rotation period. The strong peak at the third harmonic of the rotation period suggests that the rotation period of the star is consistent over the timescale of RV data collection and is consistent with the rotation period derived from the Kepler photometry.

masses of individual layers in a differentiated planet and computes the inner and outer radii of each layer. We incorporated `BurnMan` in an iterative scheme which estimates the mass of a planet with a given (relatively precisely known) radius, and specified mass distributions between the different layers (in this case, a solid metallic inner core, a liquid metallic outer core, a silicate mantle, and an outer mantle of high-pressure H_2O ice phases). The iteration begins with an educated guess for the outer radius of each layer based on a power-law scaling of the Preliminary Earth Reference Model (Dziewonski & Anderson 1981) scaling with the specified mass fractions. The mass of each layer is computed based on the outer radius of that layer and the outer radius of the underlying layer (the radius of the outermost layer is set to the known transit value), the mass fractions of each layer are then recomputed, the radii of the individual layers are adjusted based on these mass fractions, and the iteration continues until the `BurnMan`-calculated mass fractions fall within a given tolerance (0.1%) of the specified values. After convergence, the planet mass—which is the sum of the masses of the individual layers—is compared to measured values.

The silicate mantle is modeled with the EOS of magnesium-bridgmanite (Stixrude & Lithgow-Bertelloni 2011), the inner core with the EOS of solid iron (Dewaele et al. 2006), and the outer core with the EOS of liquid iron (Anderson & Ahrens 1994). The ice mantle is modeled entirely as ice VII; layers of liquid H_2O and ice Ih could exist near the surface, but would not contribute significantly (<100 km) to the planet radius. For the ice VII EOS, a third-order Birch–Murnaghan formulation was implemented (Frank et al. 2004). Ice X could exist at pressures exceeding 60 GPa (Brown & Journaux 2020),

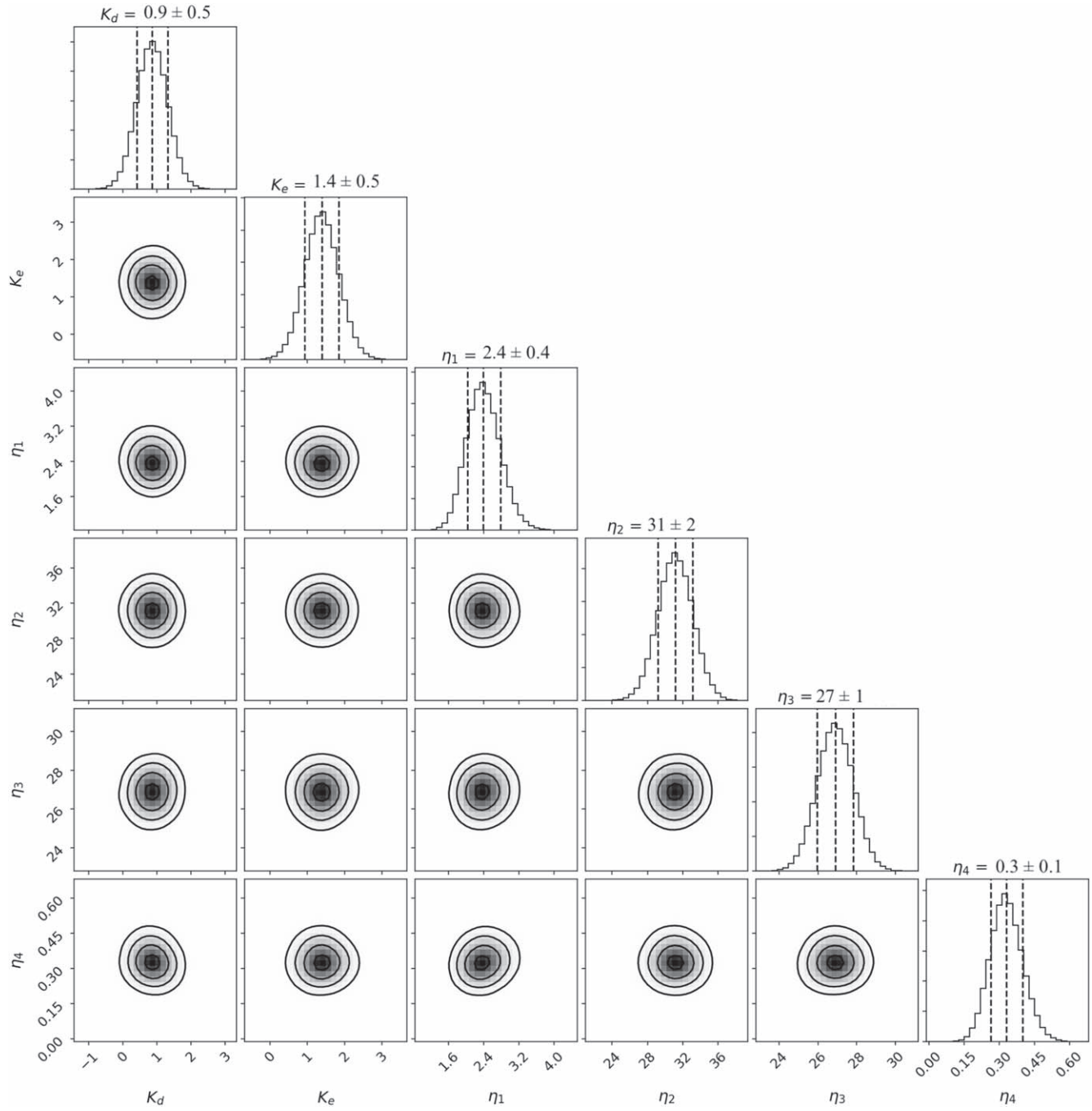

Figure 5. Corner plot showing the covariance of the semiamplitudes of Kepler-102d and Kepler-102e with the four hyperparameters from the quasiperiodic stellar noise model. The median value of each parameter is shown atop the distribution of values explored through a Markov Chain Monte Carlo algorithm plotted as a function of likelihood. The dashed lines through the distributions show the median value as well as the 1σ bounds on the parameter. The covariance plots show the likelihood of models with the parameters varying as a function of one another, and show the 0.5, 1.0, 1.5, and 2.0σ contours. K_d, K_e, and η_1 are in units of meters per second, while η_2 and η_3 are in units of days.

but the EOS of this phase is poorly constrained and so we use that of ice VII in its place. In this way, the mass of a planet with a known radius can be predicted as a function of the mass fraction of a core, silicate mantle, and ice mantle.

Figure 7 shows the range of possible compositions for Kepler-102d as a ternary diagram. The color bar shows the mass for a specified composition (as a combination of iron, silicate, and ice fractions) at the radius of the planet (from Table 2). We recovered a wide range of possible compositions for a planet of radius 1.34 $R_\oplus$, and with a mass within 2σ of our best-fit value. These are also all possible compositions consistent with the mass upper limit of $M_d < 5.3\ M_\oplus$. While the vast majority of ice, iron, and rock fractions produce planets with a mass within 2σ of our measured value, the composition that most closely reproduces a mass of 2.5 $M_\oplus$ is a planet of roughly 20% iron, 80% rock, and 0% ice by mass. This is a slightly smaller core mass fraction than the Earth (∼30% iron), but consistent with the Earth within 1σ. It is important to note, however, that the composition is highly unconstrained due to the large uncertainty on the mass measurement.

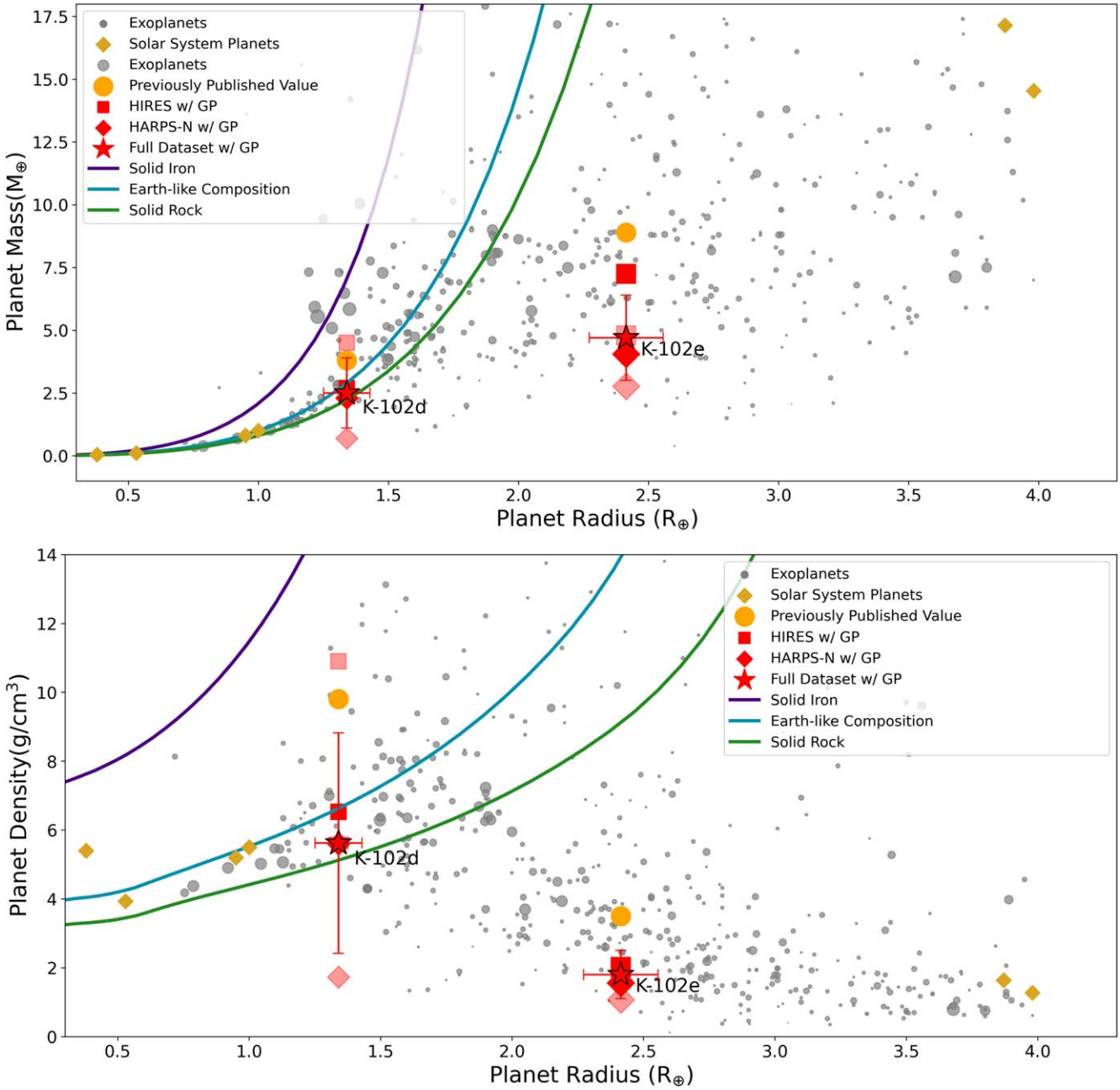

Figure 6. Mass (top panel) and density (bottom panel) are given as a function of radius for all known exoplanets with radius $R < 4\ R_{\oplus}$ that have radial velocity mass measurements (shown in gray). The size of the points (excluding Kepler-102d and Kepler-102e) scales inversely with the error of their mass measurement. The black line shows the mass–radius relation from Weiss & Marcy (2014). The density–radius curves for planets of solid iron, solid rock, and an Earth-like composition from Zeng et al. (2019) are shown, as well. Kepler-102d and Kepler-102e (K-102d and K-102e) are shown with their previous mass measurements, and for each model we explore in this paper (individual vs. combined data sets, with and without Gaussian process, GP, stellar noise modeling). For Kepler-102d, the marker for the combined data set without GP, as well as the marker for HARPS-N with GP, fall behind the marker for the full data set with GP.

For Kepler-102e, we were unable to identify a combination only of iron, rock, and ice that produces a mass within 3σ of the best-fit value. Therefore, this planet must have a nonsolid component as most sub-Neptune sized planets do, likely a gaseous envelope.

4.2. Core-envelope Model for Kepler-102e

Kepler-102e has a density consistent with other sub-Neptunes, and therefore a significant portion of the planet's radius likely comes from this atmosphere rather than a solid surface (Rogers 2015). However, a planet with this mass and radius can be estimated as having only ~2% of its mass in the H/He envelope using the relation between radius and envelope fraction from Lopez & Fortney (2014).

As a first-order approximation, we could assume that the core of the planet (the solid interior portion of the planet inclusive of rock and iron) follows the mass–radius relation for terrestrial planets:

$$R_{\rm core} \approx \left(\frac{M_{\rm core}}{M_{\oplus}}\right)^{0.25} \approx \left(\frac{M_P}{M_{\oplus}}\right)^{0.25}, \quad (4)$$

where $M_{\rm core}$ is the mass of the planet's solid core and M_P is the mass of the entire planet (Lopez & Fortney 2014). This relation

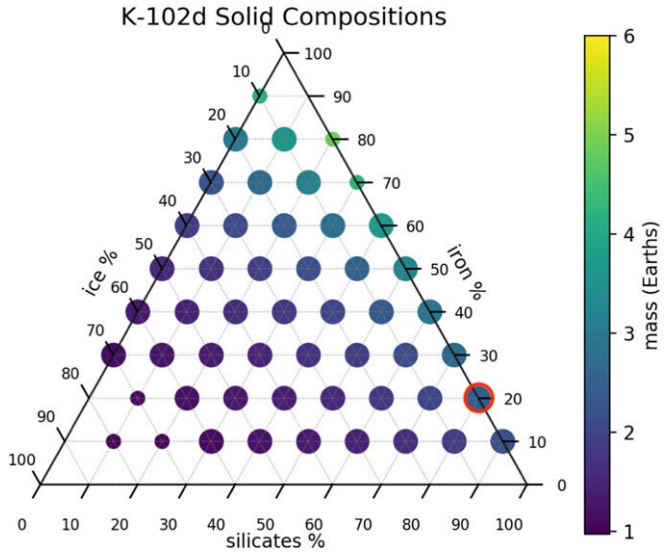

Figure 7. Ternary plot for Kepler-102d (K-102d) showing the range of possible combinations of iron, rock, and ice in increments of 10% for a planet of fixed radius. The color bar shows the resulting mass of such a planet. Masses and volumes of different substances are calculated by solving equations of state (EOS) using assumed internal pressure and temperatures using `Burnman` 0.9 (Cottaar et al. 2016). Every point corresponds to a planet with physically allowed EOS for that combination of iron, rock, and ice—and all produce values for the mass of the planet within 1σ (large points) and 2σ (small points) of our measured mass value for that planet. The horizontal dotted lines show iron fraction, the dotted lines with negative slope show ice fraction, and the lines with positive slope show silicate fraction. The red circle highlights the composition that produces our best-fit mass of $M_d = 2.5\ M_\oplus$.

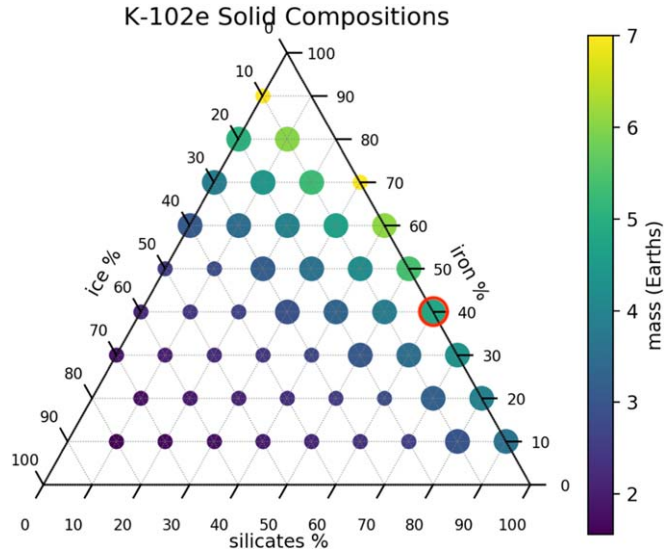

Figure 8. Ternary plot for Kepler-102e (K-102e) solid core compositions, assuming a core radius of $R_c = 1.5\ R_\oplus$. Large points represent planet compositions consistent with our measured mass of the planet to within 1σ, while smaller points represent compositions within 2σ. The planet core composition that most closely matches our measured value of $M_e = 4.7\ M_\oplus$ is one of 40% iron and 60% silicate rock—more dense than the best-fit composition for Kepler-102d.

assumes an Earth-like composition without significant quantities of water or ice. It has an inherent uncertainty of 10% when rock/iron fractions are allowed to vary.

Using this method, we can approximate the radius of the core of Kepler-102e as $R_c = 1.5\ R_\oplus$, corresponding to a density $\rho_c = 9\ \mathrm{g\ cm^{-3}}$. The results of building a core of this radius and a mass within 2σ of our best-fit value are shown in Figure 8, accounting for a 2% reduction in mass due to the envelope. Compositions within 1σ of this mass range could have silicate fractions of 0.0–0.9, iron fractions of 0.1–0.6, and ice fractions of 0.2–0.4.

This model of the core is highly uncertain, however, and does not consider significant ice fractions. Another plausible core composition is one of roughly 50% water ice and 50% rock, based on solar system abundances (Lodders 2003).

While we cannot determine the core size, we can set upper and lower limits using our `Burnman` models. Ignoring significant ice fractions in the core (Rogers 2015; Owen & Wu 2017), the largest core possible for Kepler-102e is one that lacks any iron and contains silicate rock only at $R_c = 1.6\ R_\oplus$. Considering compositions that include ice, the largest core possible for Kepler-102e is one that contains 80% ice, 10% silicate rock, and 10% iron at $R_c = 2.0\ R_\oplus$. At the other extreme, the core of Kepler-102e could be as small as $R_c = 1.2\ R_\oplus$ if made entirely of compressed iron. This puts limits on the extent of the planet's atmosphere, ranging from 16% to 50% of the planet's radius if we consider ice fractions, and 33% to 50% if we exclude ice. We can then estimate that the mass of the H/He envelope then falls between 1.8% and 4% of the total planet mass (Lopez & Fortney 2014), consistent with the assumption that the envelope mass is very small compared with the total planet mass.

4.3. Water and Ice Fractions

To investigate the plausibility of solid, differentiated planets containing significant fractions of water ice at their orbital periods, we can compute the equilibrium temperature of the planets. Assuming that a planet is radiating as a blackbody, we can calculate the equilibrium temperature of the planet as follows:

$$T_{\mathrm{Planet}} = T_*[f(1 - A_B)]^{1/4}\sqrt{\frac{R_*}{a}}. \quad (5)$$

Here, A_B is the Bond albedo, f is the reradiation factor, and a is the semimajor axis of the planet. The only unconstrained parameters are the reradiation factor and the albedo. Albedo ranges from 0.12 to 0.75 for solar system planets, while f is thought to vary from 1/4 to 2/3 (Lopez-Morales & Seager 2007).

We use the stellar properties from Table 1 and planet properties from Table 2 to calculate equilibrium temperature. Assuming they both have similar albedos to Earth (≈0.30), or even Neptune (≈0.29), it would give Kepler-102d and Kepler-102e equilibrium temperatures of ≈802 K and ≈693 K, respectively. These are well above the melting (273 K) and boiling (373 K) temperatures of water at standard temperature and pressure, and the temperature of both planets could easily be above the critical point of water (647 K; Wagner 2002). Water-rich planets that orbit close to their host star are likely to experience a runaway greenhouse effect and photodissociation of water molecules (Luger & Barnes 2015; Bolmont et al. 2017), raising the question of whether they could have retained significant water.

Unless Kepler-102e has an albedo higher than Enceladus, it would need a significant amount of atmospheric pressure to sustain liquid water or ice on the surface of the planet, on the order of 10 GPa surface pressure (Journaux et al. 2019). While we are unable to say whether or not Kepler-102e has surface oceans, compressed ice, or even water in the atmosphere, we can say this sub-Neptune-sized planet requires a substantial

gaseous envelope, and the nonsolid portion of the planet cannot be explained by water alone.

5. Conclusion

We have applied GPs to model the correlated stellar noise of Kepler-102 in both photometry from Kepler (quarters 1–17) and 146 RVs collected using HIRES and HARPS-N. This allowed us to more accurately measure the masses of two of the five transiting planets. We have determined the following:

1. Kepler-102d, a super-Earth-sized planet with a radius $R_d = 1.3 \pm 0.09\ R_\oplus$, has a mass upper limit of $M_d < 5.3\ M_\oplus$ (95% confidence). Our best fit to the RVs yields a mass $M_d = 2.5 \pm 1.4\ M_\oplus$ and a density $\rho_d = 5.6 \pm 3.2\ \mathrm{g\ cm^{-3}}$. This density is roughly half the value previously determined with the radius from Fulton & Petigura (2018) and mass from Marcy et al. (2014). It also falls within 1σ of the mass–density relations published by Otegi et al. (2020) and Weiss & Marcy (2014). The best-fit composition is ∼20% iron ∼80% silicate rock, and is consistent with an Earth-like composition, but because of the low precision achieved in the mass measurement the composition remains highly unconstrained.
2. Kepler-102e, a sub-Neptune-sized planet with a radius $2.41 \pm 0.14\ R_\oplus$, has a mass of 4.7 ± 1.7 and a density of $1.8 \pm 0.7\ \mathrm{g\ cm^{-3}}$. This density is also ∼50% smaller than the previously published value, and is consistent with other observed sub-Neptune densities. Kepler-102e has a H/He envelope likely containing ∼2%–4% of the mass of the planet. Without significant fractions of water ice, this atmosphere accounts for at least 33% of the radius of the planet. It has a minimum core size of $R_c > 1.2\ R_\oplus$, therefore giving the envelope a maximum size of 50% of the planet radius.

Characterizing activity in stars with clear rotation signals yields more robust planet masses, enabling a more realistic interpretation of planet interiors. Our study has shown that modeling stellar activity using GPs is important to derive masses and densities of small planets, particularly when there are discrepant values measured by different instruments. Using an informed estimate of the rotation period and decay timescale from the photometry is critical to ensure that the GP fit is physically motivated. GP analysis of this sort will be particularly important for more precise RV instruments such as MAROON-X, NEID, ESPRESSO/Very Large Telescope, the Keck Planet Finder, and future instruments for which stellar noise will become even more dominant over instrumental noise.

This material is based upon work supported by the National Science Foundation Graduate Research Fellowship under grant No. 1842402.

C.L.B., L.W., and D.H. acknowledge support from National Aeronautics and Space Administration (grant No. 80NSSC19K0597) issued through the Astrophysics Data Analysis Program.

D.H. also acknowledges support from the Alfred P. Sloan Foundation.

K.R. acknowledges support from the UK STFC via grant No. ST/V000594/1.

E.G. acknowledges support from NASA grant No. 80NSSC20K0957 (Exoplanets Research Program).

The HARPS-N project was funded by the Prodex Program of the Swiss Space Office (SSO), the Harvard University Origin of Life Initiative (HUOLI), the Scottish Universities Physics Alliance (SUPA), the University of Geneva, the Smithsonian Astrophysical Observatory (SAO), the Italian National Astrophysical Institute (INAF), University of St. Andrews, Queen's University Belfast, and University of Edinburgh. This work has been supported by the National Aeronautics and Space Administration under grant No. NNX17AB59G, issued through the Exoplanets Research Program.

Some of the data presented in this paper were obtained from the Mikulski Archive for Space Telescopes (MAST) at the Space Telescope Science Institute. The specific observations analyzed can be accessed via 10.17909/T9059R.

Partly based on observations made with the Italian Telescopio Nazionale Galileo (TNG) operated by the Fundación Galileo Galilei (FGG) of the Istituto Nazionale di Astrofisica (INAF) at the Observatorio del Roque de los Muchachos (La Palma, Canary Islands, Spain).

Software: Lightcurve (Lightkurve Collaboration et al. 2018), kiauhoku (Claytor et al. 2020), RadVel (Fulton et al. 2018), PyORBIT (Malavolta et al. 2016, 2018), george (Ambikasaran et al. 2015), emcee (Foreman-Mackey et al. 2013), BurnMan 0.9 (Cottaar et al. 2016), NumPy (Harris et al. 2020), Matplotlib (Hunter 2007), pandas (Wes McKinney 2010), Astropy (Astropy Collaboration et al. 2013, 2018, 2022), SciPy (Virtanen et al. 2020).

ORCID iDs

Casey L. Brinkman https://orcid.org/0000-0002-4480-310X
James Cadman https://orcid.org/0000-0002-3200-3121
Lauren Weiss https://orcid.org/0000-0002-3725-3058
Eric Gaidos https://orcid.org/0000-0002-5258-6846
Ken Rice https://orcid.org/0000-0002-6379-9185
Daniel Huber https://orcid.org/0000-0001-8832-4488
Zachary R. Claytor https://orcid.org/0000-0002-9879-3904
Aldo S. Bonomo https://orcid.org/0000-0002-6177-198X
Lars A. Buchhave https://orcid.org/0000-0003-1605-5666
Andrew Collier Cameron https://orcid.org/0000-0002-8863-7828
Rosario Cosentino https://orcid.org/0000-0003-1784-1431
Xavier Dumusque https://orcid.org/0000-0002-9332-2011
Aldo F. Martinez Fiorenzano https://orcid.org/0000-0002-4272-4272
Adriano Ghedina https://orcid.org/0000-0003-4702-5152
Andrew Howard https://orcid.org/0000-0001-8638-0320
Howard Isaacson https://orcid.org/0000-0002-0531-1073
David W. Latham https://orcid.org/0000-0001-9911-7388
Mercedes López-Morales https://orcid.org/0000-0003-3204-8183
Luca Malavolta https://orcid.org/0000-0002-6492-2085
Giuseppina Micela https://orcid.org/0000-0002-9900-4751
Emilio Molinari https://orcid.org/0000-0002-1742-7735
Ennio Poretti https://orcid.org/0000-0003-1200-0473
Alessandro Sozzetti https://orcid.org/0000-0002-7504-365X
Stéphane Udry https://orcid.org/0000-0001-7576-6236

References

Akeson, R. L., Chen, X., Ciardi, D., et al. 2013, PASP, 125, 989
Ambikasaran, S., Foreman-Mackey, D., Greengard, L., Hogg, D. W., & O'Neil, M. 2015, ITPAM, 38, 252

Anderson, W. W., & Ahrens, T. J. 1994, JGR, 99, 4273
Astropy Collaboration, Price-Whelan, A. M., Lim, P. L., et al. 2022, ApJ, 935, 167
Astropy Collaboration, Price-Whelan, A. M., Sipocz, B. M., et al. 2018, AJ, 156, 123
Astropy Collaboration, Robitaille, T. P., Tollerud, E. J., et al. 2013, A&A, 558, A33
Basri, G., & Nguyen, H. T. 2018, ApJ, 863, 190
Berger, T. A., Huber, D., Gaidos, E., & van Saders, J. L. 2018, ApJ, 866, 99
Bolmont, E., Selsis, F., Owen, J. E., et al. 2017, MNRAS, 464, 3728
Bonomo, A. S., Sozzetti, A., Santerne, A., et al. 2015, A&A, 575, A85
Bonomo, A. S., Zeng, L., Damasso, M., et al. 2019, NatAs, 3, 416
Borucki, W. J., Koch, D., Basri, G., et al. 2010, Sci, 327, 977
Brown, J. M., & Journaux, B. 2020, Minerals, 92, 10
Brown, T. M., Latham, D. W., Everett, M. E., et al. 2011, AJ, 142, 112
Bryson, S., Kunimoto, M., Kopparapu, R. K., et al. 2021, AJ, 161, 36
Chao, K.-H., deGraffenried, R., Lach, M., et al. 2021, ChEG, 81, 125735
Claytor, Z. R., van Saders, J. L., Santos, A.^, et al. 2020, kiauhoku: Stellar model grid interpolation
Cottaar, S., Heister, T., Myhill, R., Rose, I., & Unterborn, C. 2016, GGG, 15, 1164
Dai, F., Masuda, K., Winn, J. N., et al. 2019, ApJ, 883, 79
Dewaele, A., Loubeyre, P., Occelli, F., et al. 2006, PhRvL, 97, 215504
Dressing, C. D., Charbonneau, D., Dumusque, X., et al. 2015, ApJ, 800, 135
Dumusque, X., Udry, S., Lovis, C., Santos, N. C., & Monteiro, M. J. P. F. G. 2011, A&A, 525, A140
Dumusque, X., Bonomo, A. S., Haywood, R. D., et al. 2014, ApJ, 789, 154
Dumusque, X., Cretignier, M., Sosnowska, D., et al. 2021, A&A, 648, A103
Dziewonski, A. M., & Anderson, D. L. 1981, PEPI, 25, 297
Eastman, J., Gaudi, B. S., & Agol, E. 2013, PASP, 125, 83
Elkins-Tanton, L. T., & Seager, S. 2008, ApJ, 688, 628
Foreman-Mackey, D., Hogg, D. W., Lang, D., et al. 2013, PASP, 125, 306
Frank, M. R., Fei, Y., Hu, J., et al. 2004, GeCoA, 68, 2781
Fulton, B. J., & Petigura, E. A. 2018, AJ, 156, 264
Fulton, B. J., Petigura, E. A., Blunt, S., & Sinukoff, E. 2018, PASP, 130, 044504
Fulton, B. J., Petigura, E. A., Howard, A. W., et al. 2017, AJ, 154, 109
Gajdoš, P., Vaňko, M., & Parimucha, Š. 2019, RAA, 19, 041
Gibson, N. P., Aigrain, S., Roberts, S., et al. 2012, MNRAS, 419, 2683
Grunblatt, S. K., Howard, A. W., & Haywood, R. D. 2016, in IAU Proc. 29A, Astronomy in Focus (Cambridge: Cambridge Univ. Press), 208
Harris, C. R., Millman, K. J., van der Walt, S. J., et al. 2020, Nature, 585, 357
Haywood, R. D., Collier Cameron, A., Queloz, D., et al. 2014, MNRAS, 443, 2517
Howard, A. W., Johnson, J. A., Marcy, G. W., et al. 2010, ApJ, 721, 1467
Howard, A. W., Marcy, G. W., Bryson, S. T., et al. 2012, ApJS, 201, 15
Hunter, J. D. 2007, CSE, 9, 90
Journaux, B., Brown, J. M., Pakhomova, A., et al. 2019, JGR Planets, 125, e06176
Kass, R. E., & Raftery, A. E. 1995, JASS, 90, 773
Kite, E. S., Fegley, B. J., Schaefer, L., et al. 2020, ApJ, 891, 111
Kosiarek, M. R., Blunt, S., Lopez-Morales, M., et al. 2019, AJ, 157, 116
Lightkurve Collaboration, Cardoso, J. V. d., Hedges, C., et al. 2018, Lightkurve: Kepler and TESS time series analysis in Python
Liu, Y., San Liang, X., & Weisberg, R. H. 2007, JAtOT, 24, 2093
Lodders, K. 2003, ApJ, 591, 1220
Lopez, E. D. 2017, MNRAS, 472, 245
Lopez, E. D., & Fortney, J. J. 2014, ApJ, 792, 1
Lopez-Morales, M., & Seager, S. 2007, ApJL, 667, L191
Lorah, J., & Womack, A. 2019, Behavior Research Methods, 51, 440
Luger, R., & Barnes, R. 2015, AsBio, 15, 119
Malavolta, L., Nascimbeni, V., Piotto, G., et al. 2016, A&A, 588, A118
Malavolta, L., Mayo, A. W., Louden, T., et al. 2018, AJ, 155, 107
Marcy, G. W., & Butler, R. P. 1992, PASP, 104, 270
Marcy, G. W., Isaacson, H., Howard, A. W., et al. 2014, ApJS, 210, 20
Morton, T. D., Bryson, S. T., Coughlin, J. L., et al. 2016, ApJ, 822, 86
Otegi, J. F., Bouchy, F., & Helled, R. 2020, A&A, 634, A43
Owen, J. E., & Wu, Y. 2017, ApJ, 847, 29
Petigura, E. A., Howard, A. W., & Marcy, G. W. 2013, PNAS, 110, 19273
Rasmussen, C. E., & Williams, C. K. I. 2006, in Gaussian Processes for Machine Learning, ed. T. Dietterich (Cambridge, MA: MIT Press)
Rogers, L. A. 2015, ApJ, 801, 41
Rogers, L. A., & Seager, S. 2010, ApJ, 712, 974
Schröder, K.-P., Mittag, M., Hempelmann, A., González-Pérez, J. N., & Schmitt, J. H. M. M. 2013, A&A, 554, A50
Stixrude, L., & Lithgow-Bertelloni, C. 2011, GeoJI, 184, 1180
Valencia, D., Sasselov, D. D., & O'Connell, R. J. 2007, ApJ, 656, 545
van Saders, J. L., Ceillier, T., Metcalfe, T. S., et al. 2016, Nature, 529, 181
van Saders, J. L., & Pinsonneault, M. H. 2013, ApJ, 776, 67
Virtanen, P., Gommers, R., Burovski, E., et al. 2020, scipy/scipy: SciPy 1.5.3, Zenodo, doi:10.5281/zenodo.4100507
Virtanen, P., Gommers, R., Oliphant, T. E., et al. 2020, NatMe, 17, 261
Vogt, S. S., Allen, S. L., Bigelow, B. C., et al. 1994, Proc. SPIE, 2198, 362
Wagner, W., & Pruß, A. 2002, JPCRD, 31, 387
Weiss, L. M., & Marcy, G. W. 2014, ApJL, 783, L6
Weiss, L. M., Rogers, L. A., Isaacson, H. T., et al. 2016, ApJ, 819, 83
McKinney, W. 2010, in Proc. 9th Python in Science Conf., ed. S. van der Walt & J. Millman (Austin, TX: SciPy), 56
Yee, S. W., Tamayo, D., Hadden, S., & Winn, J. N. 2021, AJ, 162, 55
Zeng, L., Jacobsen, S. B., Sasselov, D. D., et al. 2019, PNAS, 116, 9723